

<https://doi.org/10.1038/s41699-025-00605-w>

# Automated device for the purification of graphene oxide dispersions: integration of cross-flow filtration and dialysis



Matheus Santos Dias<sup>1,2</sup>, Marcos Alves dos Santos<sup>3</sup>, Edvaldo Angelo<sup>1</sup>, Cecilia de Carvalho Castro Silva<sup>1,2</sup> & Camila Marchetti Maroneze<sup>1,2</sup> ✉

Graphene oxide (GO) dispersions require extensive purification to remove contaminants from synthesis. Conventional methods, such as dialysis, filtration and centrifugation are effective, but also labor-intensive, time-consuming, and challenging to automate. These approaches consume large volumes of water and energy, and limited efficiency in removing residues can compromise the properties of GO. We present a fully automated device integrating cross-flow filtration and dialysis using polyethersulfone (PES) membrane. Real-time conductivity monitoring enables optimal water exchange and resource use. The optimized system reduced conductivity from  $\sim 70$  to  $< 0.5$  mS cm<sup>-1</sup> in under 16 h for 1.0 L dispersion at 1 mg mL<sup>-1</sup>. Chemical analysis showed effective removal of ions (93% Cl<sup>-</sup>, 97% Mn<sup>2+</sup>, 92% SO<sub>4</sub><sup>2-</sup>), outperforming commercial samples. GO morphology and lateral dimensions were preserved, as verified by comprehensive characterization. This scalable platform enables high-throughput, application-ready GO purification, providing a practical solution for laboratories and industry seeking consistent, high-purity nanomaterials.

Over the past 20 years, ever since the iconic isolation of graphene in 2004 using a graphite crystal and adhesive tape<sup>1</sup>, the field of research involving this nanomaterial has undergone a remarkable transformation<sup>2,3</sup>. Initially considered as an academic curiosity, graphene quickly gained prominence due to the combination of unique electrical, mechanical, and thermal properties, which had never been observed together in a single material<sup>4–8</sup>. Within academia, multidisciplinary investigations have expanded our understanding of its fundamental characteristics, driving the development of new methods for synthesizing and modifying its structure. One notable example is the production of graphene oxide (GO) through the chemical oxidation of graphite<sup>9,10</sup>, followed by exfoliation of the bulk-layered crystal into single or ultrathin layers. From an industrial perspective, multiple practical applications have been developed, ranging from electronic devices<sup>11</sup> to anticorrosive coatings<sup>12,13</sup>, high-performance composite materials<sup>14,15</sup>, energy/electronics<sup>16,17</sup> and biomedical devices<sup>18</sup>.

Despite the fascination with the disruptive potential of 2D carbon nanomaterials for creating new technologies, one crucial obstacle is still the large-scale production of materials with similar structural and morphological characteristics to those obtained on a laboratory scale<sup>19,20</sup>. Additionally, in the specific case of GO, the purification step is often considered the major challenge for industrial production for several reasons, such as operational

complexities, large consumption of water, long process periods, and the resulting associated costs<sup>21,22</sup>. The main impurities at the end of the oxidation process include K<sup>+</sup>, Na<sup>+</sup>, Mn<sup>2+</sup>, Cl<sup>-</sup>, NO<sub>3</sub><sup>-</sup> and SO<sub>4</sub><sup>2-</sup> ions<sup>23</sup>. Eliminating these contaminants is essential to guarantee safety<sup>24</sup> and consistent performance for downstream applications<sup>25</sup> while addressing regulatory barriers for commercial uses, particularly in biotechnological or biomedical applications<sup>24,26,27</sup>.

The primary purification strategies typically employed to purify GO dispersions include centrifugation<sup>28</sup>, filtration<sup>29</sup>, and dialysis<sup>30,31</sup>. High-speed centrifugation over extended periods depends on multiple rinse cycles to eliminate soluble impurities, resulting in a bottom gel that contains substantial amounts of GO aggregates with significant re-stacking, making it challenging to re-disperse into mono- or ultrathin-layered sheets with well-preserved structure. Filtration techniques, particularly standard vacuum filtration<sup>19</sup>, offer a straightforward setup; however, the accumulation of GO flakes on the filter surface often results in the formation of compact filter cakes, which obstruct membrane flow and demand frequent maintenance, such as cleaning or replacement. Cross-flow filtration (CFF)<sup>32,33</sup>, also known as tangential flow filtration (TFF), benefits from its continuous operation, with reduced fouling and easy scalability. It is widely used in several industries, although it requires higher capital investment. Dialysis<sup>34,35</sup> uses

<sup>1</sup>Mackenzie Presbyterian University, School of Engineering, São Paulo, Brazil. <sup>2</sup>MackGrphe – Mackenzie Institute for Research in Graphene and Nanotechnologies, Mackenzie Presbyterian Institute, São Paulo, 01302-907, Brazil. <sup>3</sup>Nova analítica Importação e Exportação Ltda, São Paulo, Brazil.

✉ e-mail: [camila.maroneze@mackenzie.br](mailto:camila.maroneze@mackenzie.br)

semipermeable membranes with specific molecular weight cutoffs, which allow ions to be removed via diffusion across the membrane and is well-suited to preserve the integrity of the GO nanosheets. However, it is time-consuming and requires large volumes of ultra-pure water. Regarding automation, centrifugation is usually carried out in batch-mode cycles, partially automated, with periodic loading and unloading of the samples. CFF is comparatively more straightforward to automate and integrate into a workflow with real-time monitoring and adjustment of operational parameters. Dialysis is the least compatible with full automation and high-throughput processing due to its batch-wise nature and the extended duration required for purification. Ultimately, the successful large-scale production of GO strongly relies on the purification step, which must balance purity needs, cost, and environmental impact of the process, particularly considering the substantial consumption of ultrapure water<sup>19,22</sup>.

In this scenario, the present work describes the fabrication and performance of an automated system for the purification of GO dispersions, which is characterized by a combination of dialysis and cross-flow filtration setups. Real-time sensors and feedback loops control the operational parameters to achieve optimal processing conditions regarding water consumption, purity level, and time duration of the purification cycles. The structural and morphological properties of the resulting GO nanosheets were systematically analyzed. The high quality of the purified GO was demonstrated through comprehensive chemical and structural characterizations of the dispersion, as well as ion analysis of the main synthesis-derived contaminants. The developed system demonstrates strong potential for commercial applications, as it can be readily scaled up by adjusting the capacity of key components, such as pumps, valves, and tank, and by increasing the number of purification modules to meet larger processing demands.

## Results

### Purification mechanism

The graphene oxide samples evaluated in the present study were synthesized following a modified Hummers method<sup>9,36</sup>, which involves the chemical oxidation of natural graphite flakes using a mixture of concentrated sulfuric acid ( $\text{H}_2\text{SO}_4$ ), sodium nitrate ( $\text{NaNO}_3$ ), and potassium permanganate ( $\text{KMnO}_4$ ) under controlled temperature conditions, schematically illustrated in Fig. 1a. After completion of the oxidation reaction, the resulting GO dispersion was subjected to three successive pre-washing steps with 3.7% hydrochloric acid ( $\text{HCl}$ ) aqueous solution. Following this step, the GO was dispersed in deionized (DI) water, sonicated for 5 min, and the resulting dispersion was transferred to the developed automated purification system.

The purification cycles are governed by diffusive transport of ionic contaminants from the GO dispersion to a reservoir of pure water across a porous membrane. As schematically illustrated in Fig. 1b, the concentration

gradient drives the impurities (e.g.,  $\text{H}^+$ ,  $\text{K}^+$ ,  $\text{Cl}^-$ ,  $\text{SO}_4^{2-}$ ,  $\text{Mn}^{2+}$ ) through the membrane while GO sheets are retained. The lower panel in Fig. 1c shows a representative conductivity trace for two successive cycles: conductivity in the tank rises as the concentration of the ions increases in the water, plateaus at concentration equilibrium or water saturation, and then drops sharply when the water is replaced. This inflection point is used by the control algorithm to trigger the next cycle automatically or establish the end of the purification process.

Continuous monitoring of the tank conductivity, and thus, purification progress, is achieved with a miniaturized inline probe integrated into the lid. The sensor exhibits a linear response over the operational range of  $1.2 \times 10^{-3}$ – $3.0 \text{ mS cm}^{-1}$  (Fig. 1d;  $R^2 = 0.998$ ). A user-defined terminal conductivity ( $\kappa_{\text{target}}$ ) is uploaded at the beginning of each run. During operation, once the plateau value of any cycle reaches the  $\kappa_{\text{target}}$  for a sustained period, the software registers the process as complete, halts all pumps and valves, and displays an on-screen notification. This threshold-based end-point detection eliminates operator subjectivity and guarantees batch-to-batch consistency.

### Overview of the purification system

Regarding the need for a fully self-contained yet scalable purification platform, we have developed a compact bench-top unit that integrates all fluid-handling, sensing, and control components. A rendering is shown in Fig. 2a, b, while photographs of the actual assembled equipment can be seen in the Supplementary Material (Fig. S1A). The device couples an external water source, like a deionized water tank or a reverse-osmosis system, to a purification tank (Fig. S1B), while a separate reservoir stores the raw GO dispersion. Real-time process variables, like water conductivity and level, are visualized on a display that also allows the operator to interact with the equipment via a touchscreen interface. The frame, constructed from modular aluminum extruded profiles, provides both mechanical rigidity and the freedom to remodel the device and integrate additional modules for future scale-up. An emergency-stop (E-Stop) switch on the front panel interrupts the energy for all actuators instantaneously.

### Internal component placement and maintainability

To streamline maintenance and future upgrades, the device was engineered with a physical spatial separation between hydraulic and electronic subsystems. A cut-away rendering (Fig. 2b) shows the two diaphragm pumps ( $P_1$ ,  $P_2$ ) for water transfer, the dedicated GO recirculation pump ( $P_4$ ), and the solenoid valves ( $V_1$  /  $V_2$ ) installed on quick-release plates at the frame. All the fluid handling components are connected using autoclavable silicone hoses. The power-supply bay and electronics panel (that can be seen in Fig. S1C) are affixed to the back of the structure, isolated from the fluids path, keeping high-current wiring short and well-ventilated while leaving the front area

**Fig. 1 | Workflow from GO synthesis to automated purification.** **a** Schematic sequence of the modified Hummers route used in this study. Graphite is oxidized in concentrated  $\text{H}_2\text{SO}_4$ / $\text{NaNO}_3$ / $\text{KMnO}_4$ , diluted, quenched with  $\text{H}_2\text{O}_2$ , pre-washed three times with  $\text{HCl}$  solution, ultrasonically exfoliated in water, and finally transferred to the automated purification unit. **b** Schematic representation of the purification cycles. Panels illustrate the progressive removal of impurities during a cycle: (Stage 1) high ionic concentration at the start, (Stage 2) gradual decrease and equilibrium, and (Stage 3) cycle changing. **c** Schematic representation of the typical conductivity profile during two purification cycles, indicating the moment of water replacement. **d** Calibration curve of the inline conductivity sensor. The sensor's output voltage shows a linear correlation with conductivity values ( $1.2 \times 10^{-3}$ – $3.0 \text{ mS cm}^{-1}$ ).

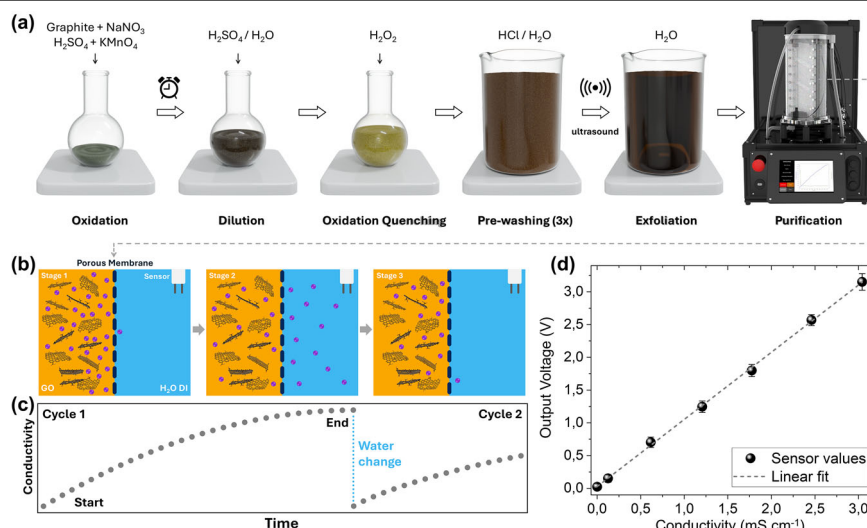
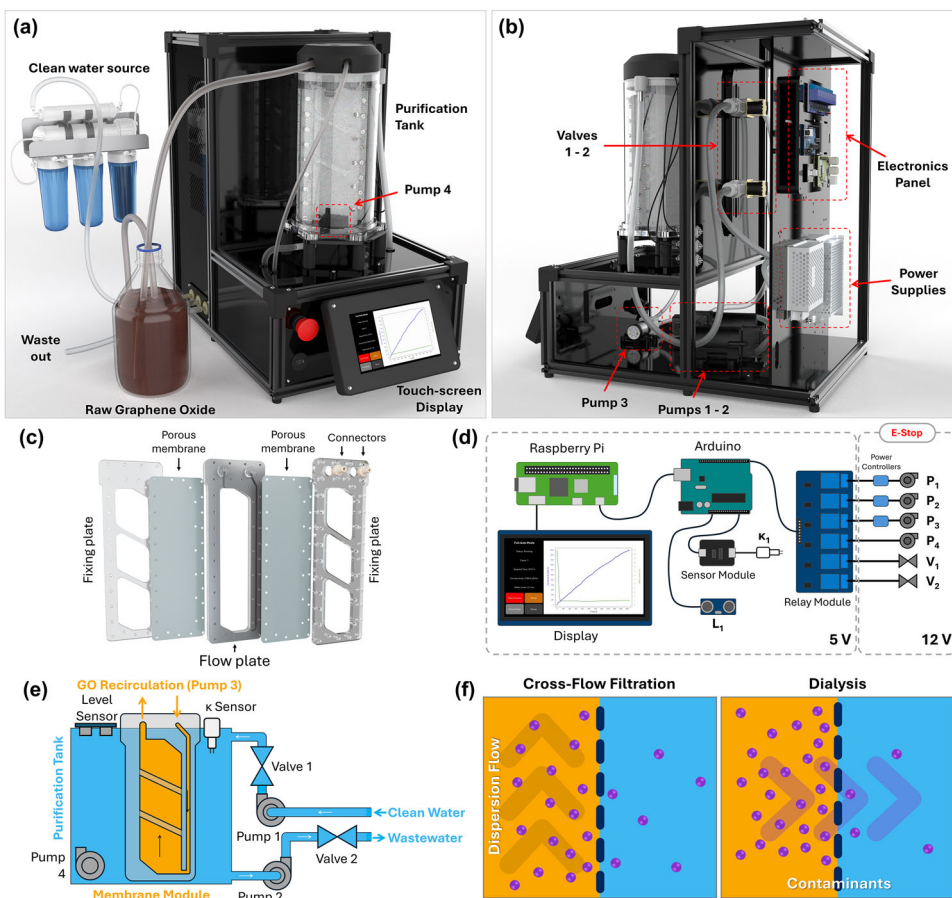


**Fig. 2 | Architecture and control framework of the automated purification system.** **a** 3D-rendered representation of the fully automated purification device connected to a clean water supply (reverse osmosis unit) and a GO dispersion container. The equipment is controlled via a touchscreen interface, which displays real-time process data. Waste is collected in a separate container. **b** Cut-away view highlighting the placement of pumps  $P_1/P_2$  (water handling), pump  $P_4$  (GO recirculation), solenoid valves  $V_1/V_2$ , the electronics back-panel, and the dual power supplies. **c** Exploded view of the membrane module assembly, showing: internal support plate, membrane sheets, external fixing plates, and PEEK connectors for fluid routing. **d** Control topology. A Raspberry Pi drives the graphical user interface and closed-loop logic, while an Arduino handles real-time sensor acquisition (conductivity probe  $\kappa_1$ , level sensor  $L_1$ ) and actuators toggling via a relay module. An emergency-stop (E-Stop) switch cuts-off 12 V power from all actuators. **e** Schematic diagram of the fluidic circuit, highlighting the purification tank. Pumps and valves regulate the flow of water and GO dispersion through the membrane module. Pump 4 enables internal recirculation of GO, while Pumps 1–3 control water flow. **f** Operating principle of the joint processes that work in the unit: tangential flow across the membrane (left) minimizes fouling, maintains a high diffusive flux and permits scaling of the system; conventional dialysis (right) is driven by the concentration gradient of the species between the dispersion and water.



unobstructed for rapid access to tubing and sensors. Photographs of the sensors and actuators used in the equipment are depicted in Fig. S2.

### Membrane module architecture

Central to the purification strategy is a high-porosity membrane cassette that combines the gentle separation principles of dialysis with the shear-controlled flow of cross-flow filtration. The sandwich-type construction depicted in Fig. 2c directs the GO dispersion through a flow plate walled by the membrane, maximizing membrane utilization while suppressing dead zones. Instead of the usual cellulose dialysis membranes with ultra-small pores (12 KDa MWCO), polyethersulfone (PES) sheets (0.1  $\mu\text{m}$  nominal pore size) were used in this equipment (preliminary experiments were made with the cellulose membrane to validate this changing of element). The membranes are clamped to both faces of the flow plate by stainless-steel bolts, yielding a leak-tight assembly that can be disassembled for cleaning or membrane replacement.

### Control electronics and automation framework

A dual-processor architecture underpins the closed-loop operation of the equipment (Fig. 2d). A Raspberry Pi microcomputer hosts the graphical user interface and executes the supervisory control algorithm, while an Arduino microcontroller performs real-time tasks such as toggling pumps and valves, debounce processing of the E-Stop switch, and high-frequency acquisition of the conductivity and level sensors. Communication between the boards is handled via serial communication. A relay module switches all pumps and valves via Arduino commands; a separate 5 V supply is used for logic electronics and a 12 V line powers the actuators, while the E-Stop button instantly de-energizes the 12 V line, guaranteeing fail-safe shutdown.

### Fluidic layout and operating concept

A dual-loop hydraulic scheme (Fig. 2e) decouples the operation of the system. Pure water is introduced into the tank by diaphragm pump  $P_1$  via solenoid valve  $V_1$  and exits through pump  $P_2$  and valve  $V_2$  to waste. Internal homogeneity on the tank is maintained by a submerged centrifugal pump ( $P_3$ ). In parallel, the GO suspension is circulated through the membrane cassette by diaphragm pump  $P_4$ , entering at the base of the cassette and exiting at the top before returning to the external reservoir. This cross-flow open path minimizes fouling and maintains a stable mass-transfer coefficient over extended runs and does not limit the volume of the dispersion that can be attached to the equipment. All four pumps and both valves are governed by an embedded control algorithm that uses live conductivity and level feedback to trigger the flow routines.

The control software executes three distinct routines: **Inflow**, when  $P_1$  and  $V_1$  admit pure water; **Recirculation**, when  $P_3$  and  $P_4$  maintain homogeneous stirring of the water and cross-flow of the GO dispersion; and **Outflow**, when  $P_2$  and  $V_2$  drain the spent water to waste. These routines are executed sequentially in fully automatic mode, though they can also be triggered individually for troubleshooting or user-defined experiments. All conductivity data and actuator states in a run are logged in the Raspberry Pi internal memory and displayed on the touchscreen interface in real-time (see Fig. S3).

### Hybrid TFF-dialysis mechanism

Fig. 2f visualizes the complementary roles of CFF and dialysis within the same membrane cassette. In the cross-flow regime (left), the GO dispersion sweeps laterally across the membrane, continually renewing the hydro-dynamic boundary layer; this suppresses material deposition, maintains a high diffusive flux, and enables straightforward scale-up by increasing channel length or stacking cassettes. Simultaneously, the classic dialysis



driving force (right) - the concentration gradient of ionic species between the dispersion and the external water loop - governs solute transport through the membrane pores. By unifying these two mass-transfer modes, the device achieves rapid impurity removal without sacrificing the gentle conditions necessary to preserve GO sheet integrity.

### Time-resolved conductivity for GO and water during purification

Figure 3a displays a representative purification run carried out in full-automatic mode for 1.0 L of a 1.0 mg mL<sup>-1</sup> GO aqueous dispersion at a flow-rate of 1350 mL min<sup>-1</sup>. The flowchart that describes the full-auto logic is displayed in Fig. S4. The upper trace (orange) shows the conductivity of the dispersion, obtained off-line with a benchtop conductometer; the lower trace (blue) is the in-situ conductivity of the tank water recorded by the inline probe. The GO conductivity decays exponentially from  $\approx 70$  mS cm<sup>-1</sup> to 0.4 mS cm<sup>-1</sup> ( $\kappa_{\text{target}}$ ) over 16 h, indicating progressive removal of contaminants. On the water side, each cycle exhibits the characteristic rise-plateau profile, shown in Fig. 1c, followed by abrupt drops when the control algorithm triggers water exchange. The synchrony of these curves confirms that the feedback logic accurately detects diffusion stabilization and minimizes downtime between cycles.

### Modeling of the cycles using Fick's Law

A detailed analysis of the data in Fig. 3b reveals that the rate of conductivity change in the water tank ( $d\kappa_w/dt$ ) decays exponentially within each cycle. This behavior can be expressed by the Fick's Law<sup>37</sup>, where the diffusive flux of impurities is proportional to the concentration gradient between the GO dispersion and the water. The kinetic model for the system can be expressed as:

$$\frac{d\kappa_w}{dt} = \frac{P_m \times A}{V_w} (\kappa_d - \kappa_w) \quad (1)$$

Here,  $P_m$  is the mass transfer coefficient,  $A$  is the membrane area,  $V_w$  is the water volume, and  $(\kappa_d - \kappa_w)$  is the instantaneous conductivity difference, which acts as the driving force. By applying a mass balance, this differential equation can be solved, yielding a theoretical model for the rate of change over time.

As shown in Fig. 3c, this theoretical model was fitted to the experimental data from the first purification cycle. The high correlation ( $R^2 = 0.998$ ) confirms that the process is well-described by a Fickian diffusion model and allows for the extraction of the system's fundamental physical parameters, such as the mass transfer coefficient,  $P_m$ .

### Development of an adaptive algorithm for cycles duration

While the physical model (Fick's Law) accurately describes a single cycle, Fig. 3b shows that the purification rate decreases with each subsequent cycle. This occurs because the initial concentration of impurities in the GO dispersion ( $\kappa_{d,0}$ ) is progressively lower. Since the initial driving force decays exponentially with each cycle, the time required to reach a fixed purification threshold ( $d\kappa_w/dt \leq 1.0$  mS cm<sup>-1</sup> h<sup>-1</sup>) is expected to grow exponentially.

This trend is experimentally confirmed in Fig. S5, which shows a clear exponential increase in the duration of successive cycles. To manage this dynamic behavior and automate the process efficiently, we developed a predictive algorithm for the cycle duration,  $t_c(x)$ :

$$t_c(x) = t_c(1) \times e^{\left(\frac{x-1}{\tau_c}\right)} \quad (2)$$

In this model, the duration of the first cycle,  $t_c(1)$ , is determined experimentally from the Fickian model analysis by finding the time at which the rate drops below the defined threshold. For the run shown in Fig. 3c, this time was found to be 0.28 h. The parameter  $\tau_c$  is the cycle time constant, which represents the characteristic number of cycles ( $x$ ) for the duration to increase by a factor of  $e$ , and is obtained by fitting the model to the data from a full run ( $R^2 = 0.996$ ).

### Performance comparison: PES versus cellulose membranes

To benchmark the high-porosity PES membrane against conventional cellulose dialysis membrane, 1.0 L of 1.0 mg mL<sup>-1</sup> GO dispersions were processed with each membrane. The conductivity decay profiles in Fig. 4a reveals a significantly faster decline for the PES system, reaching the terminal conductivity in  $16 \pm 3.5$  h versus  $39 \pm 4.2$  h for cellulose, representing a 59% decrease in the purification time. Examination of cycle-by-cycle durations (Fig. 4b) shows that both membranes complete the first five cycles rapidly ( $<1$  h), due to the high concentration gradient at this early

**Fig. 3 | Temporal variation of conductivity during purification cycles at a GO flow rate of 1350 mL min<sup>-1</sup>.** **a** Conductivity profiles of the GO dispersion (top) and the water in the purification tank (bottom) during a representative purification process using a PES membrane. The sawtooth pattern in the water conductivity curve corresponds to periodic water exchanges. **b** Evolution of tank water conductivity in each cycle, showing abrupt drops during water changes and a progressive decrease in the rate of change throughout the process. **c** Fitting of the conductivity decrease rate ( $|d\kappa/dt|$ ) during the first cycle of purification, based on the Fick's Law diffusion model.

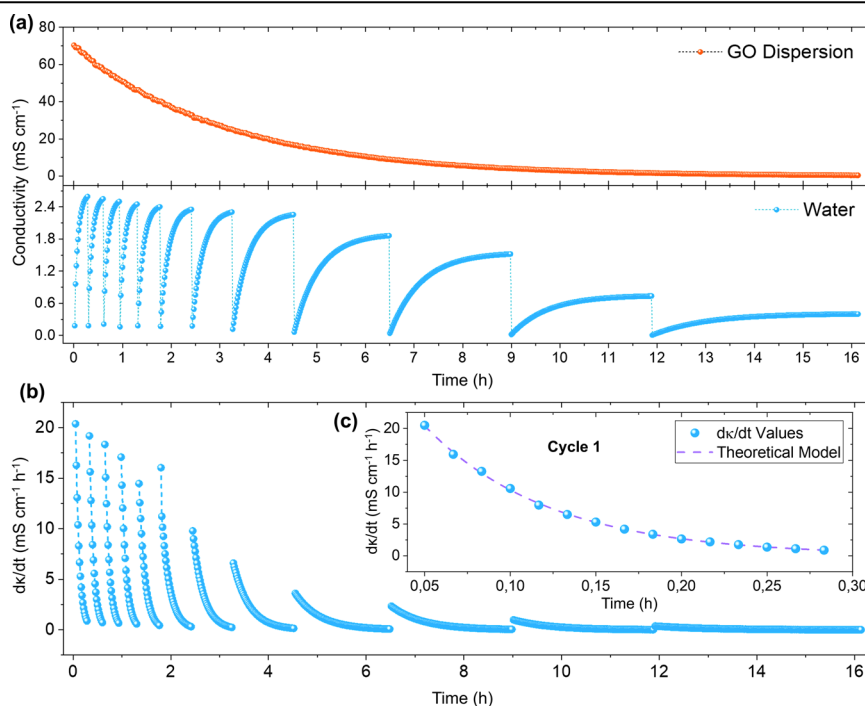


**Fig. 4 | Performance comparison.** **a** Comparison of purification performance using cellulose and PES membranes. The PES membrane significantly accelerates ionic removal due to higher permeability. **Inset:** total purification time for each membrane type. **b** Duration of each water exchange cycle for cellulose and PES membranes. With cellulose, later cycles take progressively longer, while the PES membrane maintains shorter cycle durations throughout the process. **c** Photographs of the Polyethersulfone and Cellulose membranes after use, highlighting the deposition of a GO film on their surfaces. **d** Effect of initial GO concentration on purification kinetics. Conductivity values were normalized for comparison. Faster conductivity reduction is observed with higher concentration.

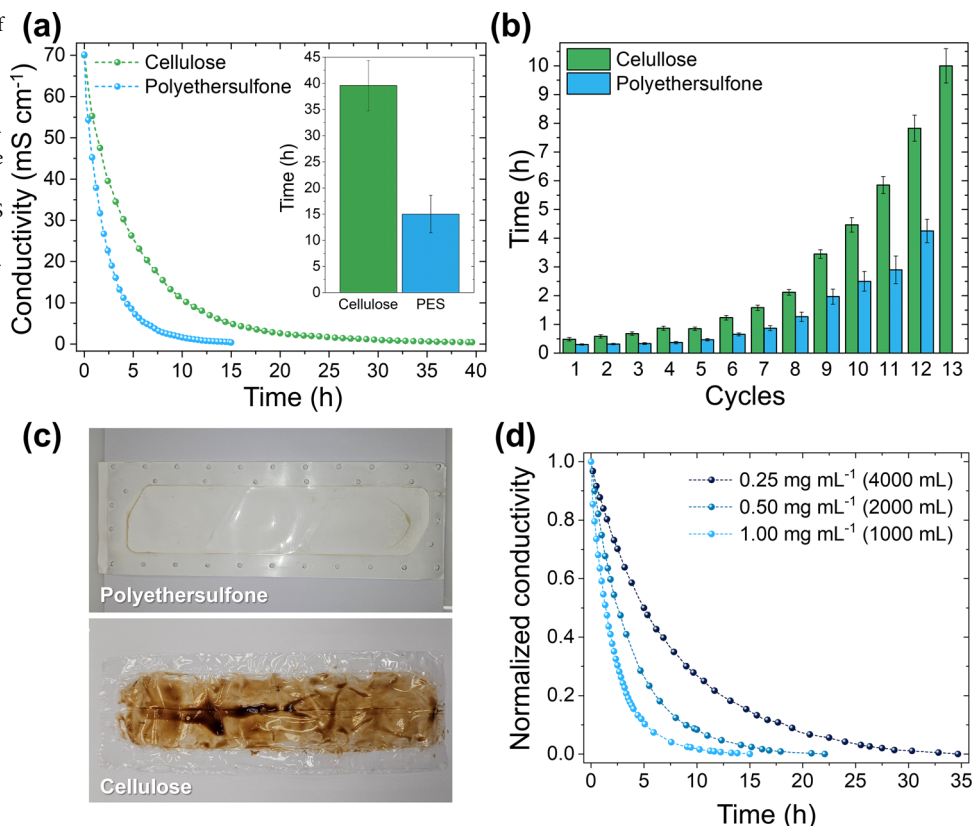


**Table 1 | Residual metal concentrations determined by ICP-OES**

| Sample           | K <sup>+</sup> (mg L <sup>-1</sup> ) | Mn <sup>2+</sup> (mg L <sup>-1</sup> ) | Na <sup>+</sup> (mg L <sup>-1</sup> ) |
|------------------|--------------------------------------|--|---------------------------------------|
| Non-Purified     | 14.08 ± 1.17                         | 17.74 ± 0.32                           | 3.74 ± 0.80                           |
| Cellulose        | 2.97 ± 0.63                          | 9.01 ± 0.04                            | 1.00 ± 0.12                           |
| Polyethersulfone | 1.18 ± 0.52                          | 1.29 ± 0.10                            | 0.50 ± 0.13                           |

stage, but the cellulose cycle time increases steeply thereafter, ultimately exceeding 10 h by the thirteenth water exchange. In contrast, the PES module levels off at ~3.5 h per cycle and requires only 12 exchanges to achieve the same purity, reflecting its higher permeation for the contaminants and resistance to fouling.

Visual inspection of the membranes after purification (Fig. 4c) explains the kinetic difference. The cellulose membrane is coated with a continuous film of GO that clogs the ultra-small pores and throttles mass transfer. No such fouling layer is observed on the PES sheet. A comparative analysis based on structural and morphological features of the membranes observed through scanning electron microscopy (SEM) helps understanding the difference in purification performance. As shown in the SEM images (Fig. S6), the PES membrane displays significantly larger pores compared to the cellulose membrane. These structural differences may have contributed to a faster purification process, as the larger pores allow for higher permeate flux and reduced hydraulic resistance. Furthermore, the surface features of the PES membrane may lead to a reduced contact area with the GO nanosheets. This property likely minimizes nonspecific adsorption and decreases membrane fouling, ultimately enhancing the long-term efficiency and stability of the purification process.

#### Influence of the GO concentration

Given that a 1.0 mg mL<sup>-1</sup> feed rapidly fouls cellulose, practical operation with that membrane often operates at lower GO concentrations. To evaluate

the trade-off, we processed equal GO masses (1.0 g) dispersed in 1000, 2000, and 4000 mL of water (initial conductivities 70, 36, and 20 mS cm<sup>-1</sup>, respectively), each starting with an initial pH value of ~0 and reaching final values of 3.8, 4.5 and 4.8, respectively, after purification using the PES module. Figure 4d plots the normalized conductivity decay,  $(\kappa - \kappa_{\text{final}}) / \kappa_{\text{initial}}$ , versus time. Diluting the dispersion from 1.00 to 0.25 mg mL<sup>-1</sup> increases the total purification time from 16 h to 35 h. With a fixed replacement volume per cycle, a larger tank dilutes the concentration gradient across the membrane and lowers the fractional removal of ions per exchange, collectively slowing the kinetics.

These findings highlight two key guidelines for scale-up: (i) *Membrane selection is critical*, a single PES cassette can accommodate higher feed concentrations without fouling, whereas cellulose membranes require pre-dilution, which ultimately prolongs the processing time; (ii) *Throughput scales with membrane area rather than tank volume*, purification efficiency is more effectively enhanced by adding parallel PES modules or increasing membrane surface area, rather than by extending the number of cycles or overall run time.

#### Chemical analyses for residual inorganic contaminants

Quantitative Inductively Coupled Plasma Optical Emission Spectroscopy (ICP-OES) analysis (Table 1) shows that purification with the PES module (samples at 1.0 mg mL<sup>-1</sup>) reduced the concentrations of Mn<sup>2+</sup>, K<sup>+</sup> and Na<sup>+</sup> by >90% compared with the non-purified batches and by 65–85% relative to the use of cellulose membrane in the purification module. In particular, manganese, often the most persistent impurity after permanganate oxidation<sup>38</sup>, was reduced from 17.7 mg L<sup>-1</sup> to 1.3 mg L<sup>-1</sup> after purification with the PES system.

According to ion chromatography data (Table 2), chloride and sulfate concentrations decreased by approximately three orders of magnitude following purification employing the PES module in the system, from 6000 mg L<sup>-1</sup> and 770 mg L<sup>-1</sup> to 17 ± 1 mg L<sup>-1</sup> and 45 ± 2 mg L<sup>-1</sup>, respectively. Nitrate levels were below the detection limit (<5 mg L<sup>-1</sup>) in both PES

**Table 2 | Residual anion concentrations determined by IC**

| Sample           | Cl <sup>-</sup> (mg L <sup>-1</sup> ) | NO <sub>3</sub> <sup>-</sup> (mg L <sup>-1</sup> ) | SO <sub>4</sub> <sup>2-</sup> (mg L <sup>-1</sup> ) |
|------------------|---------------------------------------|--|---|
| Non-Purified     | 6043 ± 5.17                           | 8.9 ± 0.9  | 771.2 ± 1.80  |
| Cellulose        | 81.8 ± 1.4                            | ND   | 146.86 ± 2.62                                       |
| Polyethersulfone | 16.8 ± 0.80                           | ND   | 44.74 ± 1.81  |

ND Not Detected, i.e., below detection range (<5 mg L<sup>-1</sup>).

and cellulose-purified samples, indicating near-complete removal. Alongside with the conductivity decay curves, these elemental data confirm that the hybrid CFF-dialysis process effectively removes both cationic and anionic residues.

Table 3 presents a comparative analysis of residual cation concentrations (K<sup>+</sup>, Na<sup>+</sup> and Mn<sup>2+</sup>) across a range of commercial graphene oxide samples, provided in both powder (P) and suspension (S) forms<sup>20</sup>, as well as samples purified using two distinct laboratory-developed methods: a microfluidic device<sup>23</sup> and the CFF-dialysis system using a PES membrane developed in this work. The data reveal that most commercial GO samples contain high levels of ionic contaminants, with potassium concentrations often exceeding 1000 mg L<sup>-1</sup>, sodium levels reaching up to 31596 mg L<sup>-1</sup> (P-017\*), and manganese levels as high as 9130 mg L<sup>-1</sup> (P-009\*). These elevated residual concentrations highlight the lack of effective purification in many commercially available GO samples, which may limit their use in sensitive applications such as biomedicine, electronics, or catalysis. In contrast, the PES-based purification platform developed in this work demonstrated remarkable removal efficiency, with reductions of up to four orders of magnitude relative to the commercial standard. The microfluidic device<sup>23</sup> also showed outstanding purification capacity, which is the lowest recorded in the entire dataset, showcasing its potential for applications requiring extremely high purity. However, it is important to note that this method is limited to very small volumes, making it impractical for routine or large-scale use.

### Characterization of purified GO

Thermogravimetric analysis (TGA) was employed to evaluate the impact of the purification process on the thermal stability and composition of GO nanosheets. The TGA curve shown in Fig. 5a for the PES purified GO sample (at concentration of 1.0 mg mL<sup>-1</sup>) revealed a characteristic multi-step decomposition profile, with an initial mass loss observed below 100 °C related to water evaporation. A second weight loss occurred between 100 and 360 °C, associated with the decomposition of oxygen-containing functional groups such as hydroxyl, epoxy, and carboxyl groups. At higher temperatures (360–600 °C) takes place the combustion of the carbon framework. The final residue at 800 °C was approximately 1.8% of the initial mass, indicating a low content of thermally stable inorganic contaminants. These results confirm that the GO sample exhibits thermal behavior consistent with high-purity graphene oxide produced by oxidative methods<sup>20,39</sup>.

XPS analysis confirmed the high chemical purity of the purified GO samples. The survey spectra (Fig. 5b) exhibited predominantly the characteristic C 1s and O 1s signals, with no relevant amount of the main impurities adsorbed on the surface of the purified GO nanosheets. The calculated C/O atomic ratio of approximately 1.86 indicates a moderate-to-high degree of oxidation, consistent with GO produced by oxidative exfoliation using strong acids and permanganate<sup>40–42</sup>. The XPS survey spectrum also shows no detectable signals from manganese (Mn 2p) or other metal contaminants (e.g., potassium or sodium), which are frequently observed in GO samples synthesized by conventional oxidative methods<sup>23,43</sup>. The absence of manganese on the GO nanosheets highlights the high efficiency of the purification strategy employed, considering that Mn residues are often challenging to remove due to their strong interactions with oxygen functionalities<sup>20</sup>. Minor S 2p (~170 eV) and N 1s (~403 eV) signals were detected, attributed to organosulfate and nitrogen-containing species covalently bonded to the GO framework during the oxidation process, in agreement with previous reports<sup>24,44–48</sup>. High-resolution analysis of the C 1s

**Table 3 | Comparison of residual cation concentrations of GO samples**

| Sample                            | K <sup>+</sup> (mg L <sup>-1</sup> ) | Na <sup>+</sup> (mg L <sup>-1</sup> ) | Mn <sup>2+</sup> (mg L <sup>-1</sup> ) |
|-----------------------------------|--------------------------------------|---------------------------------------|--|
| P-001*                            | 675                                  | 19                                    | 3163                                   |
| P-002*                            | 1751                                 | 103                                   | 4082                                   |
| P-003*                            | 647                                  | 713                                   | 6161                                   |
| P-004*                            | 1019                                 | 221                                   | 4608                                   |
| P-005*                            | –                                    | 3172                                  | 19                                     |
| P-006*                            | 628                                  | 2923                                  | 356                                    |
| P-007*                            | 1261                                 | 76                                    | 3930                                   |
| P-008*                            | 677                                  | 79                                    | 9138                                   |
| P-009*                            | 1356                                 | 32                                    | 3850                                   |
| P-010*                            | 724                                  | 920                                   | 737                                    |
| P-011*                            | 51                                   | –                                     | 104                                    |
| P-012*                            | –                                    | 47                                    | 12                                     |
| P-013*                            | 126                                  | 950                                   | 167                                    |
| P-014*                            | 83                                   | –                                     | 101                                    |
| P-015*                            | –                                    | 7                                     | 6                                      |
| P-016*                            | –                                    | 35                                    | 10                                     |
| P-017*                            | 581                                  | 31596                                 | 209                                    |
| P-018*                            | 3724                                 | 49                                    | 1274                                   |
| P-019*                            | 2704                                 | 185                                   | 756                                    |
| P-020*                            | 1131                                 | 71                                    | 12570                                  |
| P-021*                            | 2533                                 | 237                                   | 1904                                   |
| P-022*                            | 3665                                 | 3339                                  | 4068                                   |
| P-023*                            | 1164                                 | 1943                                  | 2714                                   |
| S-001*                            | 24                                   | 6                                     | 7                                      |
| S-002*                            | 4                                    | –                                     | 30                                     |
| S-003*                            | –                                    | –                                     | 1                                      |
| S-004*                            | 1168                                 | 163                                   | 3222                                   |
| S-005*                            | –                                    | 1                                     | 25                                     |
| S-006*                            | 170                                  | 1212                                  | 9385                                   |
| S-007*                            | 18                                   | –                                     | 253                                    |
| S-008*                            | –                                    | 3                                     | 0                                      |
| S-009*                            | –                                    | –                                     | 21                                     |
| S-010*                            | –                                    | –                                     | 3                                      |
| S-011*                            | 307                                  | 1172                                  | 5                                      |
| Microfluidic Device <sup>23</sup> | 0.18 ± 0.00                          | 0.03 ± 0.00                           | 0.02 ± 0.00                            |
| This Work (PES)                   | 1.18 ± 0.52                          | 0.50 ± 0.13                           | 1.29 ± 0.10                            |

\*Data from commercial GO samples extracted from Donato et al.<sup>20</sup> Samples labeled as P-xxx refer to GO received in powder form, while those labeled as S-xxx correspond to GO samples provided in suspension.

region (Fig. 5c) revealed well-defined components at characteristic binding energies. The framework peaks were assigned to C-C/C=C (sp<sup>2</sup>) at ~284.2 eV and C-C (sp<sup>3</sup>) at ~285.1 eV. The oxidized carbon species were identified at higher binding energies, with C-OH, C-O-C, and C=O functionalities at ~287.3 eV and O-C=O for the carboxyl groups at ~289.0 eV. A minor feature attributed to the π-π\* shake-up satellite was observed at ~290.7, indicative of the partial retention of aromatic domains. These results are consistent with the expected chemical structure of graphene oxide<sup>49–51</sup>.

### GO flakes morphology

Scanning Electron Microscopy (SEM) and Atomic Force Microscopy (AFM) analyses were performed to evaluate the morphological

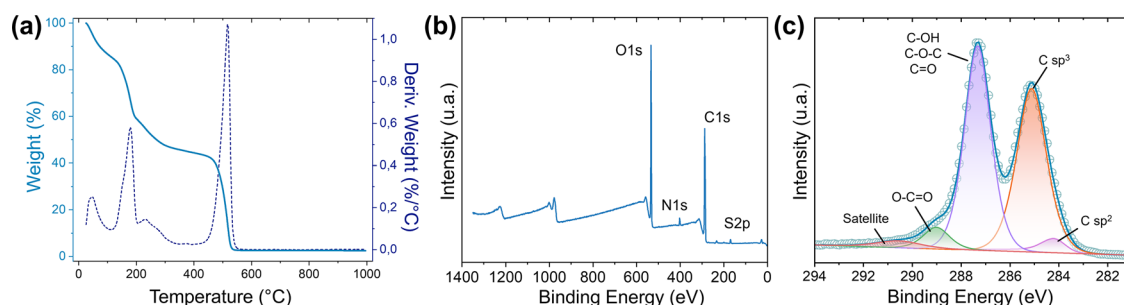


**Fig. 5 | Thermal and chemical characterizations of graphene oxide dispersions purified with the PES membrane. a** TGA curve. **b** XPS survey spectrum. **c** High-resolution C 1s XPS spectrum.

characteristics of the GO flakes ( $1.0 \text{ mg mL}^{-1}$ ) before and after purification, in order to determine whether the automated protocol affects the size or integrity of the GO sheets. The as-synthesized material (Fig. 6a,b) displays a highly polydisperse population, where micrometer-scale flakes coexist with numerous sub-micrometer fragments irregularly distributed across the substrate. After purification (Fig. 6c, d), the dispersion is dominated by well-defined flakes with lateral dimensions predominantly greater than  $5 \mu\text{m}$ , reflecting the mild nature of the purification process. The significant reduction in sub-micron debris suggests that smaller fragments pass through the  $0.1 \mu\text{m}$  PES membrane, while larger flakes are efficiently retained. No signs of mechanical damage, such as fragmentation, wrinkling, or edge delamination, were observed, indicating that the combined TFF/dialysis regime imposes minimal shear stress on the GO flakes and effectively preserves their two-dimensional structure. SEM images of the GO flakes purified by cellulose membrane are shown in Fig. S7.

AFM analysis further supports these findings by providing height-resolved confirmation of the GO thickness. As shown in Fig. 6e, a representative GO sheet exhibits a smooth topography with a step height of approximately  $0.7 \text{ nm}$  (Fig. 6f), consistent with a single-layer graphene oxide nanosheet<sup>52,53</sup>. This observation confirms the successful exfoliation of graphite oxide into monolayer GO and underscores the ability of the automated purification process to maintain flake integrity at the atomic level.

Preservation of both high aspect ratio and monolayer thickness is crucial for maximizing the mechanical reinforcement<sup>54,55</sup>, gas-barrier<sup>55,56</sup>, and percolative conductivity properties of GO in downstream applications<sup>57,58</sup>. In contrast, conventional purification methods such as high-speed centrifugation often require intermittent ultrasonication to redispersed aggregates, which can drastically reduce flake size<sup>23</sup>. Together, SEM and AFM results corroborate the conductivity and TGA data, confirming that the automated system removes ionic contaminants without compromising the intrinsic morphology or chemical quality of the graphene oxide sheets.

## Discussion

This work demonstrates the development of a fully automated benchtop purification system for graphene oxide dispersions, combining cross-flow filtration and dialysis in a compact platform.

Our results show that the main advances in purification performance, specifically the accelerated removal of ionic contaminants, reduced membrane fouling, and overall process efficiency, are primarily attributed to the intrinsic properties of the polyethersulfone membrane. Compared to conventional cellulose dialysis membranes, the PES displays larger pore size and distinctive surface morphology, which result in higher permeate flux, less adsorption, and a significantly diminished tendency for fouling. Additionally, the reduced contact area between PES and the GO sheets appears to further minimize accumulation of material at the membrane interface, enhancing long-term stability. These experimental controls confirm that the observed antifouling and kinetic behaviors are fundamentally determined by membrane material properties rather than by flow geometry or automation features alone. This improvement is achieved while preserving the

morphological integrity and lateral size of GO flakes. Analytical characterization (IC, ICP-OES, SEM, AFM, XPS, and TGA) confirmed that the automated method effectively removed ionic contaminants without inducing fragmentation or degradation, producing chemically pure, structurally preserved GO nanosheets suitable for advanced applications.

While the automation itself does not intrinsically accelerate the rate of contaminant removal, it provides substantial added value in terms of reproducibility, operational consistency, and workflow simplification. By implementing programmable routines and real-time conductivity monitoring, the platform ensures that key process steps, like water exchange, are triggered consistently and objectively, reducing operator-dependent variability. This not only facilitates standardization across users and laboratories but also enables scalable, unattended operation, which is particularly important for industrial or high-throughput settings.

Importantly, the current system establishes a foundation for more advanced, performance-driven automation. For instance, future upgrades could include real-time adaptive control of flow rates or cycle durations based on kinetic indicators such as the rate of conductivity change ( $dk/dt$ ), automated fouling diagnostics through pressure or flux sensors, or even the use of machine learning algorithms to optimize purification protocols based on historical data. Such developments would enable the transition from procedural automation to intelligent process control, providing a flexible basis for future advancements in intelligent process control.

## Methods

### Materials

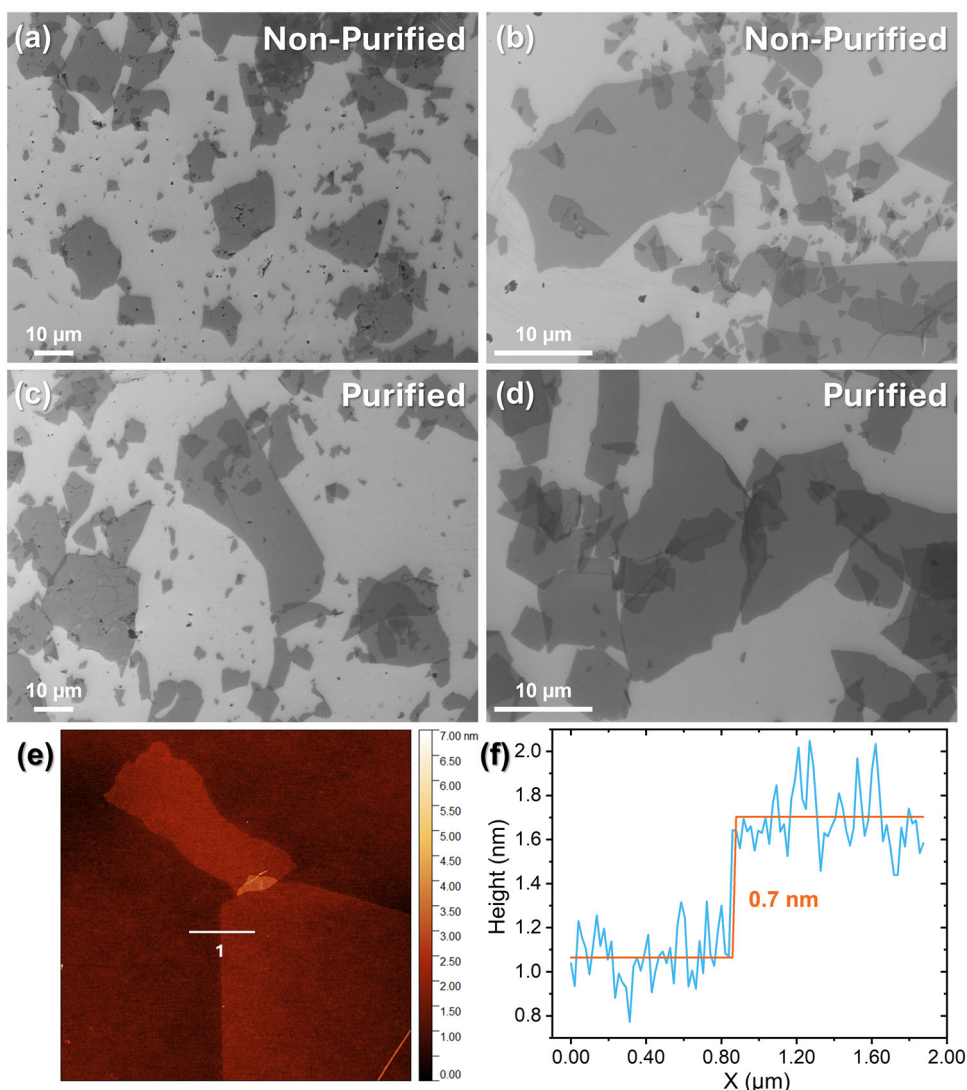
Natural graphite was purchased from Nacional do Grafite (Graflake 9980. Carbon content  $\approx 99.4\%$ , Flake size  $\approx 180 \mu\text{m}$ ).  $\text{KMnO}_4$  ( $\geq 99.0\%$ ) and  $\text{NaNO}_3$  ( $\geq 99.0\%$ ) were purchased from Sigma-Aldrich.  $\text{H}_2\text{SO}_4$ ,  $\text{H}_2\text{O}_2$  ( $35.0\%$ ) and  $\text{HCl}$  ( $37.0\%$ ) were supplied by Synth. Deionized water from a Merck-Millipore system ( $18.2 \text{ M}\Omega\text{cm}$  at  $25^\circ\text{C}$ ) was used for the syntheses and sample preparations. Reverse-osmosis filtered water from a Gehaka OS20LXE system was used for the purification of GO. Dialysis membrane ( $12 \text{ kDa}$  Molecular Weight Cut-Off) was purchased from Sigma-Aldrich and polyethersulfone (PES) filtration membrane ( $0.1 \mu\text{m}$ ) was supplied by GVS.

### GO synthesis

The graphene oxide dispersion was obtained by the modified Hummers method as described in the literature<sup>9</sup>.  $1.0 \text{ g}$  of graphite flakes were added to a flask followed by  $0.75 \text{ g}$  of  $\text{NaNO}_3$  and  $40 \text{ mL}$  of  $\text{H}_2\text{SO}_4$  under stirring. After  $30 \text{ min}$ , the system was placed in an ice bath and  $4.5 \text{ g}$  of  $\text{KMnO}_4$  was added in small fractions over a period of  $1 \text{ h}$ . The system was maintained under stirring at room temperature for  $72 \text{ h}$ . The flask was then placed in an ice bath and  $100 \text{ mL}$  of  $\text{H}_2\text{SO}_4$  aqueous solution ( $0.14\%$ ) was added in parts over  $1 \text{ h}$  and kept under stirring for  $2 \text{ h}$ . After that,  $3.0 \text{ mL}$  of  $35\% \text{ H}_2\text{O}_2$  was slowly added to the suspension, followed by  $2 \text{ h}$  of stirring. The material was then washed 3 times with  $\text{HCl}$  aqueous solution ( $3.7\%$ ) and finally dispersed in  $1 \text{ L}$  of deionized water, followed by sonication at  $37 \text{ kHz}$  for  $5 \text{ min}$  to allow the exfoliation of graphite oxide into graphene oxide nanosheets.



**Fig. 6 | SEM images of GO flakes before and after purification and AFM of a PES purified sample.** a, b GO dispersion prior to purification. c, d GO purified using the automated system with a PES membrane. e, f AFM of the purified dispersion.



### GO characterizations

Thermal stability and oxidation degree were evaluated on a TA Instruments SDT-600 simultaneous TGA/DSC system. Approximately 10 mg of dried GO was placed in an alumina crucible and heated from 20 °C to 1000 °C at 5 °C min<sup>-1</sup> under a constant synthetic air flow (100 mL min<sup>-1</sup>).

Elemental composition and surface chemical states were analyzed with a Thermo Scientific K-Alpha spectrometer (Al Kα radiation, 1486.6 eV; spot size 300 μm). Survey scans (0–1350 eV) were acquired at 200 eV pass energy, step of 0.1 eV and 10 cycles. The high-resolution scans of C 1 s were acquired at 50 eV pass energy, step of 0.01 eV and 10 cycles.

GO morphology was examined on a JEOL JSM-7800 F field-emission SEM operated at an accelerating voltage of 0.3 keV. Aqueous GO dispersions (1 μg mL<sup>-1</sup>) were drop-cast onto silicon wafers and dried under vacuum prior to imaging.

### Analytical techniques

Metal ions (K<sup>+</sup>, Mn<sup>2+</sup>, Na<sup>+</sup>) were quantified via ICP-OES on a Thermo Scientific iCAP Pro XP ICP-OES equipped with a high-resolution Echelle polychromator, CID detector, concentric nebulizer and cyclonic spray chamber. Plasma power, nebulizer gas flow, auxiliary gas flow and peristaltic-pump speed were auto-optimized by Qtegra™ ISDS software and are summarized in Table S1. To ensure high-precision quantifications, the wavelengths were selected based on: (i) the highest intensity observed in the central pixels; (ii) the lowest background radiation detected in the pixels to

the left and right of the emission peak; and (iii) the lowest relative standard deviation (RSD) across triplicate measurements (n = 3). Based on these criteria, the spectral lines selected for quantification were K I 766.490 nm, Mn I 276.482 nm, and Na I 588.995 nm. Samples were diluted 10-fold with 2% HNO<sub>3</sub> and analyzed in triplicate; concentrations were calculated from the linear regression equations provided in Table S2. The samples were diluted 10x for the analyses.

Anions (Cl<sup>-</sup>, NO<sub>3</sub><sup>-</sup>, SO<sub>4</sub><sup>2-</sup>) were determined using a Thermo Scientific Inuvion-RFIC system fitted with an IonPac AG19/AS19 column set, KOH eluent generation and suppressed conductivity detection. The eluent flow was 0.25 mL min<sup>-1</sup>; the KOH gradient is listed in Table S3. Calibration curves (5–80 mg L<sup>-1</sup>) were prepared from a multi-anion stock solution (Thermo Dionex, 100 mg L<sup>-1</sup>) and yielded R<sup>2</sup> > 0.999 for all species (Table S4). Samples were injected in triplicate after dilution (100x, 10x, 1x for Non-Purified, Cellulose and PES respectively).

### Device fabrication and assembly

The purification module was constructed using a transparent acrylic tube (150 mm inner diameter) with a total internal volume of 3.6 L. The bottom of the tank was sealed with a 10 mm thick acrylic plate, while the lid was custom-fabricated via 3D printing to hold a level sensor (HC-SR04) and an inline fluid electrical conductivity sensor (Gravity TDS/EC, DFRobot). This configuration enabled real-time monitoring of the purification progress and water levels during operation.



The membrane module followed a layered design, consisting of a 6 mm-thick acrylic flow plate sandwiched between two 2 mm acrylic spacers, with the membranes mounted on both external faces. The stack was clamped by 10 mm outer plates and tightened with stainless-steel M4x30 mm bolts. CNC-machined PEEK connectors were threaded into the outer plates to provide reliable tubing interfaces for fluid entry and exit; flexible silicone hoses were used throughout the entire flow circuit, both for GO and water, to couple the ports to the pumps, valves, and reservoirs.

### Electronics

The operation of the equipment is managed by an integrated control system consisting of an Arduino microcontroller and a Raspberry Pi computer. The Arduino interfaces directly with relays responsible for actuating pumps and valves, as well as receiving input signals from the integrated sensors. Communication between the Arduino and the Raspberry Pi is established via serial protocol, enabling data exchange and command synchronization. The Raspberry Pi is connected to a touchscreen display, for graphical user interface that allows real-time monitoring, control, and interaction.

Electrical power is supplied from two independent DC power sources: a 5 V (5 A) supply dedicated to powering the Arduino, Raspberry Pi, and associated electronics, and a 12 V (15 A) source utilized for the higher-current demands of the pumps and valves. Additionally, the system incorporates an emergency stop button mounted on the front panel, designed to interrupt power delivery to all actuators when activated. To further enhance operational flexibility, three controllers are integrated, allowing adjustment of the flow rates through pumps  $P_1$ ,  $P_2$ , and  $P_4$ , and ensuring adaptable operation tailored to specific purification requirements.

### Control software and operating modes

A hierarchical control architecture was implemented on the Raspberry Pi–Arduino pair to accommodate manual, semi-automatic, and fully automatic operation. In manual mode, each pump and solenoid valve are toggled directly from the touchscreen, permitting point-to-point verification of the hydraulic circuit. Semi-automatic mode exposes individual routines (Inflow, Recirculation and Outflow) as one-touch macros. Fully automatic mode executes these routines in a closed-loop sequence: an inflow step commences when either the tank level reaches approximately 3.5 L; recirculation continues until the time-averaged conductivity derivative  $|dk/dt|$  drops below  $5.0 \mu\text{S cm}^{-1} \text{ min}^{-1}$ ; the outflow step is initiated automatically and stops after emptying of the tank. Upon conductivity curve stabilizing around the user-defined terminal conductivity ( $\kappa_{\text{target}}$ ), the system issues an audible alarm and halts all actuators, if not, the cycle repeats until the meeting of this criterion.

### Calibration of the inline conductivity probe

Calibration of the conductivity probe was carried out at  $23 \pm 0.5^\circ\text{C}$  using seven NaCl standards (1.2, 126, 616, 1206, 1775, 2460, and  $3042 \mu\text{S cm}^{-1}$ ) prepared from analytical-grade salt (Sigma Aldrich) and verified on a Metrohm 914 benchtop meter. The probe was immersed in each solution under gentle stirring, rinsed with ultrapure water between measurements, and logged at 1 Hz for 60 s via the Arduino's 10-bit ADC. The average voltage (V) of each series was fitted to a linear model, yielding the calibration equation

$$\kappa = 975.7 V - 26.4 (R^2 = 0.998) \quad (3)$$

where  $\kappa$  is the solution conductivity. Voltages below 0.03 V (sensor noise floor) were clipped to zero in firmware to avoid non-physical negative conductivities. The calibrated coefficients are uploaded at start-up and applied in real time during automated runs (Fig. 2b).

### Purification runs and conductivity monitoring

Experiments were performed at  $23 \pm 1^\circ\text{C}$  using PES or cellulose dialysis membranes assembled into the same hydraulic circuit. GO dispersions were prepared at the final concentration of 1.00, 0.50 and  $0.25 \text{ mg mL}^{-1}$  in ultrapure water, each containing exactly 1.0 g of GO. Inline water

conductivity was logged at 0.0167 Hz via the calibrated probe. Dispersion conductivity was determined off-line every 20 min with a Metrohm 914 conductivity meter (cell constant  $1.0 \text{ cm}^{-1}$ ), positioned constantly inside the GO reservoir.

The flow rates used during the tests were  $1350 \text{ mL min}^{-1}$  for the GO dispersion and approximately  $3700 \text{ mL min}^{-1}$  for the water. It is important to note, however, that the water flow generated by pump  $P_4$  is not directly comparable to the flow of the GO dispersion. This is because  $P_4$  is positioned inside the tank and serves primarily to promote fluid turbulence and stirring, rather than to drive a continuous flow as in the case of the dispersion.

### Data availability

The authors declare that the data supporting the findings of this study are available within the paper and its supplementary information file. Should any raw data files be needed in another format, they are available from the corresponding author upon request.

Received: 12 July 2025; Accepted: 3 September 2025;

Published online: 29 September 2025

### References

- Novoselov, K. S. et al. Electric field effect in atomically thin carbon films. *Science* **306**, 666–669 (2004).
- Zhao, Y. & Lin, L. Graphene, beyond lab benches. *Science* **386**, 144–146 (2024).
- Peplow, M. Coming of age. *Science* **386**, 138–143 (2024).
- Balandin, A. A. et al. Superior thermal conductivity of single-layer graphene. *Nano Lett.* **8**, 902–907 (2008).
- Bolotin, K. I. et al. Ultrahigh electron mobility in suspended graphene. *Solid State Commun.* **146**, 351–355 (2008).
- Frank, I. W., Tanenbaum, D. M., Van Der Zande, A. M. & McEuen, P. L. Mechanical properties of suspended graphene sheets. *J. Vac. Sci. Technol. B Microelectron. Nanometer Struct. Process. Meas. Phenom.* **25**, 2558–2561 (2007).
- Ghosh, S. et al. Extremely high thermal conductivity of graphene: Prospects for thermal management applications in nanoelectronic circuits. *Appl. Phys. Lett.* **92**, 151911 (2008).
- Lee, C., Wei, X., Kysar, J. W. & Hone, J. Measurement of the elastic properties and intrinsic strength of monolayer graphene. *Science* **321**, 385–388 (2008).
- Hirata, M., Gotou, T., Horiuchi, S., Fujiwara, M. & Ohba, M. Thin-film particles of graphite oxide 1. *Carbon* **42**, 2929–2937 (2004).
- Stankovich, S. et al. Synthesis of graphene-based nanosheets via chemical reduction of exfoliated graphite oxide. *Carbon* **45**, 1558–1565 (2007).
- Eda, G. & Chhowalla, M. Chemically derived graphene oxide: towards large-area thin-film electronics and optoelectronics. *Adv. Mater.* **22**, 2392–2415 (2010).
- Aramayo, M. A. F. et al. Eco-friendly waterborne polyurethane coating modified with ethylenediamine-functionalized graphene oxide for enhanced anticorrosion performance. *Molecules* **29**, 4163 (2024).
- Cui, G. et al. A comprehensive review on graphene-based anti-corrosive coatings. *Chem. Eng. J.* **373**, 104–121 (2019).
- Stankovich, S. et al. Graphene-based composite materials. *Nature* **442**, 282–286 (2006).
- Huang, X., Qi, X., Boey, F. & Zhang, H. Graphene-based composites. *Chem. Soc. Rev.* **41**, 666–686 (2012).
- Krishnan, D. et al. Energetic graphene oxide: Challenges and opportunities. *Nano Today* **7**, 137–152 (2012).
- Rocha, J. F. et al. Graphene oxide fibers by microfluidics assembly: a strategy for structural and dimensional control. *Nanoscale* **13**, 6752–6758 (2021).
- Georgakilas, V. et al. Noncovalent functionalization of graphene and graphene oxide for energy materials, biosensing, catalytic, and biomedical applications. *Chem. Rev.* **116**, 5464–5519 (2016).

19. Nishina, Y. Mass production of graphene oxide beyond the laboratory: bridging the gap between academic research and industry. *ACS Nano* **18**, 33264–33275 (2024).
20. Donato, K. Z. et al. Graphene oxide classification and standardization. *Sci. Rep.* **13**, 6064 (2023).
21. Abdel-Motagaly, A. T., El Roubay, W. M. A., El-Dek, S. I., El-Sherbiny, I. M. & Farghali, A. A. Fast technique for the purification of as-prepared graphene oxide suspension. *Diam. Relat. Mater.* **86**, 20–28 (2018).
22. Tölle, F. J., Gamp, K. & Mülhaupt, R. Scale-up and purification of graphite oxide as intermediate for functionalized graphene. *Carbon* **75**, 432–442 (2014).
23. Santos, M. A., Marques, L. & Silva, C. D. C. C. Purification of graphene oxide dispersions by using a fluidic cell. *Anal. Methods* **12**, 3575–3581 (2020).
24. Barbolina, I. et al. Purity of graphene oxide determines its antibacterial activity. *2D Mater.* **3**, 025025 (2016).
25. Faria, A. F., Perreault, F. & Elimelech, M. Elucidating the role of oxidative debris in the antimicrobial properties of graphene oxide. *ACS Appl. Nano Mater.* **1**, 1164–1174 (2018).
26. Ali-Boucetta, H. et al. Purified graphene oxide dispersions lack in vitro cytotoxicity and in vivo pathogenicity. *Adv. Healthc. Mater.* **2**, 433–441 (2013).
27. Mrózek, O. et al. Salt-washed graphene oxide and its cytotoxicity. *J. Hazard. Mater.* **398**, 123114 (2020).
28. Tene, T. et al. Toward large-scale production of oxidized graphene. *Nanomaterials* **10**, 279 (2020).
29. Ceriotti, G., Romanchuk, A. Y., Slesarev, A. S. & Kalmykov, S. N. Rapid method for the purification of graphene oxide. *RSC Adv.* **5**, 50365–50371 (2015).
30. Chen, J., Li, Y., Huang, L., Li, C. & Shi, G. High-yield preparation of graphene oxide from small graphite flakes via an improved Hummers method with a simple purification process. *Carbon* **81**, 826–834 (2015).
31. Mikheev, I. V. et al. High-throughput preparation of uncontaminated graphene-oxide aqueous dispersions with antioxidant properties by semi-automated diffusion dialysis. *Nanomaterials* **12**, 4159 (2022).
32. Alhourani, A. H., Cashman, J. & Schöne, K. An Improved Method to Wash Graphene Prior to Use as a Drug Delivery Vehicle. Application Note, Sartorius Lab Instruments GmbH & Co. Available at: <https://www.sartorius.com/download/947254/vivaflow-graphene-application-note-en-l-sartorius-pdf-data.pdf> (2021).
33. Li, C., Guo, Y., Shen, L., Ji, C. & Bao, N. Scalable concentration process of graphene oxide dispersions via cross-flow membrane filtration. *Chem. Eng. Sci.* **200**, 127–137 (2019).
34. Bhunia, P., Kumar, M. & De, S. Rapid and efficient removal of ionic impurities from graphene oxide through hollow fiber diafiltration. *Sep. Purif. Technol.* **209**, 103–111 (2019).
35. Bhunia, P., Kumar, M. & De, S. Fast purification of graphene oxide solution by continuous counter current hollow fibre dialysis: A step towards large scale production. *Can. J. Chem. Eng.* **97**, 1596–1604 (2019).
36. Hummers, W. S. & Offeman, R. E. Preparation of graphitic oxide. *J. Am. Chem. Soc.* **80**, 1339–1339 (1958).
37. Bird, R. B., Stewart, W. E. & Lightfoot, E. N. Transport Phenomena. (J. Wiley and sons, New York Chichester Brisbane [etc.], 1960).
38. Ye, R. et al. Manganese deception on graphene and implications in catalysis. *Carbon* **132**, 623–631 (2018).
39. Farivar, F., Lay Yap, P., Karunagaran, R. U. & Losic, D. Thermogravimetric analysis (TGA) of graphene materials: effect of particle size of graphene, graphene oxide and graphite on thermal parameters. *C J Carbon Res* **7**, 41 (2021).
40. Jiříčková, A., Jankovský, O., Sofer, Z. & Sedmidubský, D. Synthesis and applications of graphene oxide. *Materials* **15**, 920 (2022).
41. Al-Gaashani, R., Najjar, A., Zakaria, Y., Mansour, S. & Atieh, M. A. XPS and structural studies of high quality graphene oxide and reduced graphene oxide prepared by different chemical oxidation methods. *Ceram. Int.* **45**, 14439–14448 (2019).
42. Yu, H., Zhang, B., Bulin, C., Li, R. & Xing, R. High-efficient synthesis of graphene oxide based on improved hummers method. *Sci. Rep.* **6**, 36143 (2016).
43. Dimiev, A. M. & Tour, J. M. Mechanism of graphene oxide formation. *ACS Nano* **8**, 3060–3068 (2014).
44. Pattisson, S. et al. Tuning graphitic oxide for initiator- and metal-free aerobic epoxidation of linear alkenes. *Nat. Commun.* **7**, 12855 (2016).
45. Aixart, J., Díaz, F., Llorca, J. & Rosell-Llompart, J. Increasing reaction time in Hummers' method towards well exfoliated graphene oxide of low oxidation degree. *Ceram. Int.* **47**, 22130–22137 (2021).
46. Al-Gaashani, R. et al. Effects of preparation temperature on production of graphene oxide by novel chemical processing. *Ceram. Int.* **47**, 10113–10122 (2021).
47. Guo, S., Garaj, S., Bianco, A. & Ménard-Moyon, C. Controlling covalent chemistry on graphene oxide. *Nat. Rev. Phys.* **4**, 247–262 (2022).
48. Ikram, R., Jan, B. M. & Ahmad, W. An overview of industrial scalable production of graphene oxide and analytical approaches for synthesis and characterization. *J. Mater. Res. Technol.* **9**, 11587–11610 (2020).
49. Kovtun, A. et al. Accurate chemical analysis of oxygenated graphene-based materials using X-ray photoelectron spectroscopy. *Carbon* **143**, 268–275 (2019).
50. Marciano, D. C. et al. Improved synthesis of graphene oxide. *ACS Nano* **4**, 4806–4814 (2010).
51. Perrozzi, F., Prezioso, S. & Ottaviano, L. Graphene oxide: from fundamentals to applications. *J. Phys. Condens. Matter* **27**, 013002 (2015).
52. Loh, K. P., Bao, Q., Eda, G. & Chhowalla, M. Graphene oxide as a chemically tunable platform for optical applications. *Nat. Chem.* **2**, 1015–1024 (2010).
53. Dreyer, D. R., Park, S., Bielawski, C. W. & Ruoff, R. S. The chemistry of graphene oxide. *Chem. Soc. Rev.* **39**, 228–240 (2010).
54. Palermo, V., Kinloch, I. A., Ligi, S. & Pugno, N. M. Nanoscale mechanics of graphene and graphene oxide in composites: a scientific and technological perspective. *Adv. Mater.* **28**, 6232–6238 (2016).
55. Smith, A. T., LaChance, A. M., Zeng, S., Liu, B. & Sun, L. Synthesis, properties, and applications of graphene oxide/reduced graphene oxide and their nanocomposites. *Nano Mater. Sci.* **1**, 31–47 (2019).
56. Yoo, B. M., Shin, H. J., Yoon, H. W. & Park, H. B. Graphene and graphene oxide and their uses in barrier polymers. *J. Appl. Polym. Sci.* **131**, app39628 (2014).
57. Dong, L., Yang, J., Chhowalla, M. & Loh, K. P. Synthesis and reduction of large sized graphene oxide sheets. *Chem. Soc. Rev.* **46**, 7306–7316 (2017).
58. Dideikin, A. T. & Vul', A. Y. Graphene oxide and derivatives: the place in graphene family. *Front. Phys.* **6**, 149 (2019).

## Acknowledgements

This study was founded by Coordination for the Improvement of Higher Education Personnel (CAPES), Mackenzie Research and Innovation Fund (MackPesquisa, 231019), National Council for Scientific and Technological Development (CNPq) (grant No. 408248/2023-8, 313091/2022-6 and 147825/2023-7) and Financiadora de Estudos e Projetos (Finep) (Grant No. 1151/22).

## Author contributions

M.S.D: Conceptualization, data curation, formal analysis, investigation, methodology, visualization, writing – original draft. M.A.S: Methodology. E.A.: Conceptualization. C.C.C.S: Conceptualization, validation, writing – review & editing. C.M.M: Conceptualization, funding acquisition, project administration, supervision, validation, writing – original draft, writing – review & editing. All authors reviewed the manuscript.

## Competing interests

The authors declare no competing interests.

## Additional information

**Supplementary information** The online version contains supplementary material available at

<https://doi.org/10.1038/s41699-025-00605-w>.

**Correspondence** and requests for materials should be addressed to Camila Marchetti Maroneze.

**Reprints and permissions information** is available at <http://www.nature.com/reprints>

**Publisher's note** Springer Nature remains neutral with regard to jurisdictional claims in published maps and institutional affiliations.

**Open Access** This article is licensed under a Creative Commons Attribution-NonCommercial-NoDerivatives 4.0 International License, which permits any non-commercial use, sharing, distribution and reproduction in any medium or format, as long as you give appropriate credit to the original author(s) and the source, provide a link to the Creative Commons licence, and indicate if you modified the licensed material. You do not have permission under this licence to share adapted material derived from this article or parts of it. The images or other third party material in this article are included in the article's Creative Commons licence, unless indicated otherwise in a credit line to the material. If material is not included in the article's Creative Commons licence and your intended use is not permitted by statutory regulation or exceeds the permitted use, you will need to obtain permission directly from the copyright holder. To view a copy of this licence, visit <http://creativecommons.org/licenses/by-nc-nd/4.0/>.

© The Author(s) 2025